Edge modes of chiral Berry plasmons in graphene nanoribbons

Ya Zhang,[1,*] Jianguo Gu,[2] and Feng Zhai[3,†]
[1]*Department of Physics, Wuhan University of Technology, Wuhan 430070, China*
[2]*School of Physics, Huazhong University of Science and Technology, Wuhan 430074, China*
[3]*Department of Physics, Zhejiang Normal University, Zhejiang 321004, China*

(Received 11 November 2018; revised manuscript received 24 April 2019; published 28 May 2019)

This study examines the edge modes of chiral Berry plasmons propagating along zigzag or armchair edges of a graphene nanoribbon under a finite Berry flux and Fermi pressure. A two-dimensional quantum hydrodynamic model is used to derive analytical expressions of the dispersion relation and transverse confinement length. Direction-dependent edge modes exist in armchair nanoribbons under antisymmetric or symmetric boundary conditions. A confined mode appears in the zigzag nanoribbon under hard-wall boundary conditions. The transverse confinement length of edge plasmons in the nanoribbon can be an order of magnitude shorter than that in the semi-infinite structure.

DOI: 10.1103/PhysRevB.99.195450

I. INTRODUCTION

An edge plasmon was first reported on a liquid-helium surface with external magnetic fields based on a linearized fluid model [1,2]. Subsequently, edge magnetoplasmons were studied numerically in the same electron system where the nearby grounded metal plate was considered [3]. Recently, edge plasmons have attracted increasing interest in graphene. Kumada *et al.* [4] investigated edge magnetoplasmons in graphene using high-frequency electronic measurements, which promotes the use of graphene for future edge plasmonic devices. Principi *et al.* [5] have reported two oppositely directed acoustic edge plasmon modes occurring at the boundary of a graphene film modulated by strain-induced pseudomagnetic fields. This type of confinement may be further improved by applying nanostructures [6]. Silvestrov *et al.* [7] analytically calculated charge accumulation at the boundaries of a graphene strip induced by a gate voltage, and they predicted that electron-electron interaction yielded charge confinement on the graphene edges. Several experimental works have observed edge plasmons in graphene nanoribbon (GNR) structures. Poumirol *et al.* [8] investigated edge magnetoplasmons in quasineutral epitaxial GNRs subject to a perpendicular magnetic field. They found that plasmonic losses were suppressed under an external magnetic field. This phenomenon contrasts that in a conventional two-dimensional electron gas (2DEG). In fact, edge-plasmon excitation has been shown to have a longer lifetime under high magnetic fields in GNRs [9]. By using nano-infrared imaging techniques, Fei *et al.* [10] investigated plasmon confinement in GNRs on Al_2O_3 substrates, where the plasmon modes under zero magnetic field depend on the ribbon width and infrared frequency. Nikitin *et al.* [6] investigated the near-field structure of surface and edge plasmons in GNRs with scattering-type scanning near-field optical microscopy for real-space imaging of surface or edge plasmons, which allowed the observation of ultraconfined resonating edge modes.

Two basic shapes are possible for graphene edges in GNRs: zigzag and armchair edges [11,12]. Nakada and Fujita [13] employed a nearest-neighbor tight-binding model to predict the existence of edge electron states in GNRs with general edges consisting of mixtures of both zigzag and armchair sites. The analytical wave function and energy dispersion have been derived for zigzag and armchair edges [14,15]. Their work indicates that all zigzag GNRs are metallic with confined edge electron states, whereas armchair GNRs are either metallic or insulating, depending on the ribbon width. For bulk plasmons in various GNRs, the dispersion relation and edge-dependent reflection have been studied [16–21]. Furthermore, Nikitin *et al.* [22] predicted that GNRs can support surface and edge-plasmon modes within the random-phase approximation. Song *et al.* [23] predicted the existence of chiral Berry plasmons (CBPs) and nonreciprocal chiral edge modes in a semi-infinite system with a nonzero Berry flux under zero magnetic field. We further investigated the edge modes of CBPs in gapped graphene by using a quantum hydrodynamic (QHD) model [24].

However, chiral edge plasmons in GNRs with zigzag (ZZ) or armchair (AC) edges have yet to be characterized. The objective of this paper is thus to demonstrate how boundary conditions affect the existence of chiral or confined edge plasmons. We consider gapped graphene with a nonzero Berry flux and various boundary conditions. The analytical dispersion relations in ZZ and AC nanoribbons are derived. The appearance of nonreciprocal edge modes is discussed for different edges. This work predicts a one-way propagating edge-plasmon mode in AC GNRs with antisymmetric or symmetric boundary conditions. A confined mode propagates unidirectionally in the ZZ GNR with the hard-wall boundary condition. In GNRs with a small ribbon width, the frequencies of edge-plasmon modes and confined modes are always lower than the bulk plasmon frequency. These results are in

*yazhang@whut.edu.cn
†fzhai@zjnu.cn

contrast to those in a semi-infinite structure [23,24] where counterpropagating edge modes exist and edge-plasmon dispersion can intersect the bulk plasmon dispersion. We also discuss how ribbon width and the Berry flux affect the frequency and lateral confinement length of edge plasmons. For edge-plasmon modes in AC GNR under symmetric boundary condition and confined modes in ZZ GNR, the transverse confinement length is about an order of magnitude shorter than that in a semi-infinite structure. The effect of Berry flux on the edge modes depends on the edge type, which cannot be revealed from a semi-infinite system.

II. MODEL AND FORMALISM

We adopt the QHD model to investigate edge plasmons in graphene nanoribbons. The QHD model has been developed by solving the Wigner-Poisson kinetic model or the Schrödinger-Poisson system [25,26], which can effectively capture the essential features of a quantum electron gas. The explicit descriptions of the macroscopic variables in QHD, such as density and momentum, were derived from the first two moments of the Wigner function integrated over the velocity space, which make it easier to interpret the terms of fluid quantities that are employed in classical physics. The QHD model has been used in many works [25–28]. Haas *et al.* [25] used the QHD model to investigate two-stream instability, where the dispersion relation possesses a semiclassical branch and two quantum branches. Manfredi *et al.* [26] used the QHD model to describe the stationary states of a quantum electron gas and the two-stream instability. They found that the quantum effect reduced the region of instability. Garcia *et al.* [27] adopted the QHD model to discuss the suppression of four-wave instability. Shukla [29] employed the QHD model to study electron-ion-dust plasmas, where a dispersion relation for a new dust mode was derived. The QHD model was also used to calculate the energy loss of charged particles [30,31]. Recently, a nonlinear dispersion relation of low frequency wave in degenerate plasmas was derived in the homogeneous quantum dusty magnetoplasmas based on the QHD model [32].

We consider a 2DEG in GNRs with ZZ or AC edges in the (x, y) plane (see Fig. 1). The 2DEG is fully degenerate at zero temperature and subject to a finite Berry flux. The ZZ nanoribbon has top and bottom edges at $y = \mp L/2$, and the AC nanoribbon has left and right edges at $x = \mp L/2$, where L is the width of the GNR.

A linearized QHD model [24–26,33] is applied to describe plasmon motion in GNRs:

$$0 = \frac{\partial n_{e1}}{\partial t} + n_0 \nabla \cdot \mathbf{V}, \tag{1}$$

$$\frac{\partial \mathbf{u}_e}{\partial t} = \frac{e}{m^*}\nabla\phi - \frac{v_F^2}{n_0}\nabla n_{e1} + \frac{\hbar^2}{4m^* 2n_0}\nabla(\nabla^2 n_{e1}), \tag{2}$$

$$\phi(\mathbf{r}, t) = \int d^2\mathbf{r}' W(\mathbf{r} - \mathbf{r}') n_{e1}(\mathbf{r}', t). \tag{3}$$

Here, $\nabla = \frac{\partial}{\partial x}\mathbf{e_x} + \frac{\partial}{\partial y}\mathbf{e_y}$, $n_{e1} = n_e - n_0$ is the two-dimensional electron density fluctuation, n_0 is the equilibrium density of the 2DEG, $v_F = 1 \times 10^8$ cm/s is the Fermi velocity [34], $m^* = \hbar\sqrt{\pi n_0}/v_F$ is the plasmon mass [34], e is the elementary charge, $\hbar$ is the reduced Planck constant, ϕ is the electrostatic potential, $W(\mathbf{r} - \mathbf{r}')$ is the Coulomb interaction, and $\mathbf{u}_e$ is the mean fluid velocity. The total velocity field $\mathbf{V}$ consists of not only the fluid component $\mathbf{u}_e$ but also an additional anomalous velocity $\mathbf{V}_a$ due to the nonzero Berry flux [23],

$$\mathbf{V} = \mathbf{u}_e + \mathbf{V}_a, \mathbf{V}_a = \frac{eF}{n_0\hbar}[\nabla\phi \times \mathbf{e}_z], \tag{4}$$

where $F = \sum_i \int d^2\mathbf{k}\, \Omega_i(\mathbf{k}) f_i^0(\mathbf{k})/(2\pi)^2$ is the dimensionless Berry flux [35,36], and $f_i^0(\mathbf{k})$ and $\Omega_i(\mathbf{k})$ are, respectively, the equilibrium occupancy and Berry curvature for band i. The form of $\Omega_i(\mathbf{k})$ is given in Refs. [35,36].

The certification of the QHD model is discussed in detail in our previous work [24]. On the right-hand side of Eq. (2), the first term is the electrostatic force, the second term is the zero-temperature Fermi pressure due to the Pauli exclusion principle [33], and the third term is the quantum diffraction pressure induced by the Bohm force [33]. For definiteness, the quantum diffraction pressure is omitted, because our numerical results indicate that the effect of this term is indeed negligible in the considered range of wave vector. Finally, the damping effect is not considered in Eq. (2), because the Pauli blocking could suppress it [26,37].

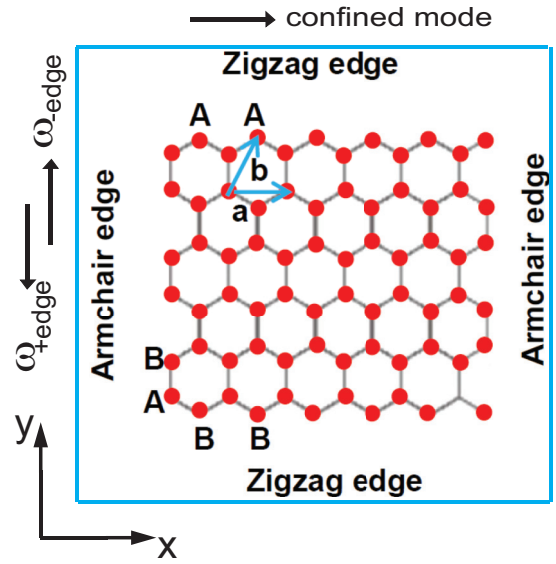

FIG. 1. Schematic illustration of a graphene nanoribbon with zigzag edges (top and bottom) and armchair edges (left and right). Under a finite Berry flux and Fermi pressure, chiral edge plasmons propagate along the armchair edges with direction-dependent frequency $\omega_{\pm edge}$, whereas a confined mode exists along the zigzag edges. Antisymmetric or symmetric boundary conditions are imposed on armchair edges [38,39], while hard-wall boundary conditions are imposed on zigzag edges [14,15,40]. The primitive lattice vectors (blue arrows) are $\mathbf{a} = \mathbf{a_0}(1, 0)$ and $\mathbf{b} = \mathbf{a_0}(1/2, \sqrt{3}/2)$, where $a_0 = 0.246$ nm is the graphene lattice constant.

A. One unified constraint equation of edge plasmons

We find a unified constraint equation for the edge plasmons with propagating wave vector k and frequency ω. Near the

boundary $y = \mp L/2$, edge plasmons are given as

$$\begin{aligned}\phi(\mathbf{r},t) &= \phi_k(y)\exp(i\omega t - ikx),\\ n_{e1}(\mathbf{r},t) &= n_{e1k}(y)\exp(i\omega t - ikx),\\ u_e(\mathbf{r},t) &= u_{ek}(y)\exp(i\omega t - ikx),\\ \mathbf{V}(\mathbf{r},t) &= \mathbf{V}_k(y)\exp(i\omega t - ikx),\\ W(\mathbf{r},t) &= W_k(y)\exp(i\omega t - ikx).\end{aligned} \tag{5}$$

For a GNR with boundary $y = \mp L/2$, $\mathbf{V}(\mathbf{r},t)$ is generally finite for $|y| \leqslant L/2$ but vanishes for $|y| > L/2$. A jump condition of $\partial_y\phi_k(y)$ is derived [23] by replacing $n_{e1}(\mathbf{r}) = -n_0\nabla\cdot\mathbf{V}(\mathbf{r},t)/i\omega$ in Eq. (3). At the boundary $y = \mp L/2$, using the identity

$$\partial_y \mathbf{V}_y(y)\mid_{y=(\mp L/2)^{\pm}} = \mathbf{V}_y\mid_{y=(\mp L/2)^{\pm}}\delta(y \pm L/2), \tag{6}$$

one gets

$$\begin{aligned}&\left.\frac{\partial\phi_k}{\partial y}\right|_{y=(\mp L/2)^+} - \left.\frac{\partial\phi_k}{\partial y}\right|_{y=(\mp L/2)^-}\\ &= -\frac{1}{i\omega}\left[\left.\frac{\partial W_k(y\pm L/2)}{\partial y}\right|_{y=(\mp L/2)^-}\right.\\ &\quad\left.-\left.\frac{\partial W_k(y\pm L/2)}{\partial y}\right|_{y=(\mp L/2)^+}\right] n_0\mathbf{V}_y\mid_{y=(\mp L/2)^{\pm}}.\end{aligned} \tag{7}$$

Note that the jump condition in the above equation depends on the perpendicular velocity at the edges, $\mathbf{V}_y\mid_{y=(\mp L/2)^{\pm}}$, where the subscript $(\mp L/2)^{\pm}$ represents that the velocity should be evaluated in the region of the GNR. Here $q/k \ll k_F = \sqrt{\pi n_0}$ (k_F is the Fermi wave number). In this long-wavelength limit [2,23], W_k can be approximated as

$$\begin{aligned}W_k(y) &\approx -4\pi\frac{e}{\kappa}\int\frac{dq}{2\pi}\frac{|k|}{q^2+2k^2}\exp(iqy)\\ &= -\frac{4\pi e}{2\sqrt{2}\kappa}\exp(-\sqrt{2}|ky|).\end{aligned} \tag{8}$$

Here q describes the wave vector in x (perpendicular to the boundary), and κ is the background dielectric constant. A justification of Eq. (8) together with the detailed derivation of Eqs. (9)–(12) is given in the Appendix. With this approximated form of $W_k(y)$, from Eqs. (3) and (5) we find

$$\begin{aligned}&\left(\partial_y^2 - 2k^2\right)\phi_k(y) = 4\pi(e/\kappa)|k|n_{e1k}(y),\ |y| \leqslant L/2,\\ &\left(\partial_y^2 - 2k^2\right)\phi_k(y) = 0,\ |y| > L/2.\end{aligned} \tag{9}$$

Applying $\partial/\partial t$ to the continuity equation [Eq. (1)] and substituting $\frac{\partial\mathbf{V}}{\partial t} = \frac{\partial\mathbf{u}_e}{\partial t} + \frac{\partial\mathbf{V}_a}{\partial t}$ into the resulting identity, we obtain

$$\frac{\partial^2 n_{e1}}{\partial t^2} = -\frac{e}{m^*}n_0\nabla^2\phi + \frac{\pi\hbar^2 n_0}{m^{*2}}\nabla^2 n_{e1}. \tag{10}$$

The electron density fluctuation $n_{e1}(\mathbf{r},t)$ can be expressed in terms of $\phi_k(y)$ from Eq. (9),

$$n_{e1}(\mathbf{r},t) = \kappa\frac{\left(k_n^2 - 2k^2\right)}{4\pi e|k|}\phi_k(y)\exp(i\omega t - ikx). \tag{11}$$

Here, ik_n is a real (purely imaginary) wave vector for which $\partial_y^2\phi_k(y) = k_n^2\phi_k(y)$ holds in the region $|y| < L/2$. The value of k_n depends on the boundary condition (see the following subsections B and C). By substituting Eq. (11) into Eq. (10), we derive

$$1 = \frac{2[\omega_P(k)]^2}{\omega^2}\frac{k_n^2 - k^2}{k_n^2 - 2k^2} - A_S\frac{k_n^2 - k^2}{\omega^2}, \tag{12}$$

where $\omega_P(k) = [2\pi n_0 e^2|k|/(m^*\kappa)]^{1/2}$ is the two-dimensional (2D) bulk plasmon frequency [2,23] in the absence of the Fermi pressure and Berry flux terms, and $A_S = \pi\hbar^2 n_0/m^{*2}$ is the coefficient of the Fermi pressure term.

The derivation of the constraint equation (12) for the boundary $y = \mp L/2$ can be applied for the boundary $x = \mp L/2$ after exchanging the x and y coordinates in all the above expressions. This equation is derived from coupling the continuity and momentum balance equations [Eqs. (1) and (2)] with the definitions of edge plasmon waves [Eq. (5)]. We also utilize the property of the edge plasmon $\nabla^2\phi = (k_n^2 - k^2)\phi$, which holds for all considered boundary conditions. Therefore, Eq. (12) is indeed independent of the specific edge of ZZ GNR or AC GNR. In Eq. (12) the edge-plasmon frequency ω and the wave vector k_n are unknown for a given propagating wave vector k. To determine the dispersion relation of the edge plasmons, one needs another constraint equation that depends on the boundary condition of $\phi_k(y)$, which will represent the unique character of the ZZ and AC edges.

Here the boundary conditions used for the wave function of electrons are used for the electric potential ϕ. The physical reason is that it is possible to combine Eqs. (1) and (2) into an effective Schrödinger equation. Indeed, let us define the effective wave function, $\psi = \sqrt{n_e}\exp(iS/\hbar)$, where $n_e = |\psi|^2$, and S is the phase related to the mean fluid velocity u_e. The electron density is determined by the effective wave function (ψ), while the electric potential (ϕ) is produced by the electron density fluctuation $n_{e1} = n_e - n_0$. Since the electric potential and the density fluctuation have the same form of plasmon wave shown in Eq. (5), the boundary conditions used for the wave function of electrons can be used for the electric potential.

B. Edge-plasmon mode in armchair nanoribbons

Both edges of an AC GNR are an admixing of atoms belonging to different sublattices. Based on Refs. [38,39], an antisymmetric or symmetric boundary condition is imposed on the AC edges so that the solution of Eq. (9) can be written as (after exchanging the x and y coordinates)

$$\begin{aligned}&\phi_k(x) = \phi_0\exp(\kappa_0 x), \quad x < -L/2,\\ &\phi_k(x) = \phi_1[\exp(k_n x) + s\exp(-k_n x)], \quad |x| \leqslant L/2,\\ &\phi_k(x) = \phi_2\exp(-\kappa_0 x), \quad x > L/2,\end{aligned} \tag{13}$$

where $s = 1$ ($s = -1$) under the symmetric (antisymmetric) boundary conditions, $\kappa_0 = \sqrt{2}|k|$, ϕ_0, ϕ_1, and ϕ_2 are real, and k_n is either real or purely imaginary [14,15,34]. When k_n is positive, the ratio $|\phi_k(x = \pm L/2)|/|\phi_k(x \to 0)|$ tends to ∞ as $L \to \infty$, indicating an edge mode.

By using the boundary condition of continuous ϕ, the jump condition (7), and Eq. (13), one yields the second transcendental equation that ω and k_n satisfy. Under the antisymmetric

boundary condition ($s=-1$), it is

$$\left[1+\frac{\omega_p^2(k)}{\omega^2}-A_S\frac{k_n^2-2k^2}{\omega^2}\right]k_n\cosh(k_nL/2)+\left[\sqrt{2}|k|-A_F\frac{k^2\mathrm{sgn}(k)}{\omega}\right]\sinh(k_nL/2)=0. \quad (14)$$

Here, $A_F=4\pi e^2F/\kappa\hbar$ is the coefficient of the chiral Berry term. Under the symmetric boundary condition ($s=1$), this transcendental equation becomes

$$0=\left[1+\frac{\omega_p^2(k)}{\omega^2}-A_S\frac{k_n^2-2k^2}{\omega^2}\right]k_n\sinh(k_nL/2)+\left[\sqrt{2}|k|+A_F\frac{k^2\mathrm{sgn}(k)}{\omega}\right]\cosh(k_nL/2). \quad (15)$$

For a given wave vector k and under antisymmetric (symmetric) boundary conditions, the two nonlinear equations (12) and (14) [(12) and (15)] are solved numerically to calculate the edge-plasmon frequency ω together with the wave vector k_n. Due to the presence of a term $\propto \mathrm{sgn}(k)$ in Eqs. (14) and (15), the propagating velocity of the edge plasmon depends on the propagating direction [23]. The frequency of a forward-propagating (backward-propagating) edge-plasmon mode is defined as $\omega_{-\mathrm{edge}}$ ($\omega_{+\mathrm{edge}}$) for $k>0$ ($k<0$). The calculation predicts that the $\omega_{-\mathrm{edge}}$ mode exists under antisymmetric boundary conditions, while the $\omega_{+\mathrm{edge}}$ mode appears under symmetric boundary conditions. Under the antisymmetric boundary condition and the long-wavelength limit $k\to 0^+$, one has

$$k_n(k\to 0^+)=\frac{\sqrt{2}\omega_p(k)}{\sqrt{1.3A_S}},$$
$$\omega_{-\mathrm{edge}}(k\to 0^+)=\frac{2}{3}\omega_p(k). \quad (16)$$

Under symmetric boundary conditions, $\omega_{+\mathrm{edge}}$ and k_n have the long-wavelength limit

$$k_n(k\to 0^-)=|k|,$$
$$\omega_{+\mathrm{edge}}(k\to 0^-)=L\omega_p^2(k)/A_F. \quad (17)$$

C. Confined plasmon mode in zigzag nanoribbons

Each edge of a ZZ GNR consists of atoms in the same sublattice (A for the top edge and B for the bottom edge). According to Refs. [14,15,40], we adopt a hard-wall boundary condition on ZZ edges so that $\mathbf{V}(y=\pm L/2)\equiv 0$, which is actually a homogeneous Dirichlet boundary condition on $\mathbf{V}(\mathbf{r},t)$. In this case, the solution of $\phi_k(y)$ in the region $|y|\leqslant L/2$ can be written as [14,15,40]

$$\phi_k(y)=\phi_1\sin(ik_ny), \quad (18)$$

where ϕ_1 and ik_n are real. After some algebra, one obtains the second constraint equation on ω and k_n, which reads

$$0=\left[\frac{\omega_p^2(k)}{\omega^2}-A_S\frac{k_n^2-2k^2}{\omega^2}\right]k_n\cos(k_nL/2)-A_F\frac{k^2\mathrm{sgn}(k)}{\omega}\sin(k_nL/2). \quad (19)$$

This solution of Eqs. (12) and (19) is called the "confined edge mode" in Refs. [14,15,34].

Note that there is no confined plasmon mode in the AC GNR even under the hard-wall boundary condition $\mathbf{V}(y=\pm L/2)\equiv 0$, which agrees with the theoretical prediction [15,34] and experimental observation [41]. In this situation the bulk solution of $\phi_k(x)$ in the GNR region has the form $\phi_1\cos(k_nx)$ or $\phi_1\sin(k_nx)$, where k_n is real. Substituting this solution into the hard-wall boundary condition, one obtains

$$0=\left[\frac{\omega_p^2(k)}{\omega^2}-A_S\frac{k_n^2-2k^2}{\omega^2}\right]k_n\sin(k_nL/2)-A_F\frac{k^2\mathrm{sgn}(k)}{\omega}\cos(k_nL/2). \quad (20)$$

Since the set of equations (12) and (20) has no real solution of k_n and ω, no confined mode exists in the AC nanoribbon.

III. RESULTS AND DISCUSSIONS

In this section, we show the numerical results of the dispersion relation and transverse confinement length for the edge modes in the AC GNR and confined modes in the ZZ GNR, where the MATLAB solver function is used. The electron density in equilibrium and the background dielectric constant are taken to be the same as in Ref. [23]: $n_0=6\times 10^{10}$ cm^{-2} and $\kappa=1$. The plasmon frequency ω and wave number k are in units of $E_F/\hbar$ and k_F, respectively, where $E_F=\hbar v_Fk_F$ is the Fermi energy. The dimensionless Berry flux F is fixed at $F=1$ without specification. The ribbon width is in units of the lattice constant of graphene $a_0=0.246$ nm.

The dispersion relations for edge plasmons in AC GNR are shown in Figs. 2(a) and 2(b) where the ribbon width is $L=24a_0$. The results are compared to the bulk plasmon frequency ω_{P}. It is evident that the one-way acoustic edge mode exists in AC GNRs under both antisymmetric and symmetric boundary conditions. These edge modes are induced by the Fermi pressure and Berry flux. The finite Berry flux brings chirality into the dispersion relation [Eqs. (14) and (15)], which depends on the sign of the wave number k. The zero-temperature Fermi pressure due to the Pauli exclusion principle breaks the space-reversal symmetry, where fermions are described by antisymmetric states. An antisymmetric two-particle state is regarded as a sum of states with one particle in a forward-propagating state while the other is in a backward-propagating state. The total antisymmetric wave function changes sign under space reversal, yielding the singularity of nonlinear Eqs. (12) and (14) [Eqs. (12) and (15)]. This scenario induces a frequency gap for $k\leqslant 0$ ($k\geqslant 0$) under antisymmetric (symmetric) boundary conditions. Under antisymmetric boundary conditions, the edge plasmon propagates only along the $-y$ direction and has a long-wavelength limit $\omega_{-\mathrm{edge}}\propto\sqrt{|k|}$ [Eq. (16)]. Under symmetric boundary conditions, the edge plasmon propagates only along the $+y$ direction. In the long-wavelength limit, $\omega_{+\mathrm{edge}}(k)\propto|k|$ [Eq. (16)] is much smaller than $\omega_{-\mathrm{edge}}(-k)$.

In Fig. 2(c) the dispersion of confined plasmon mode is plotted for a ZZ GNR with width $L=1212.5a_0$ under the hard-wall boundary conditions. The confined plasmon mode is only forward-propagating. Its dispersion curve is almost

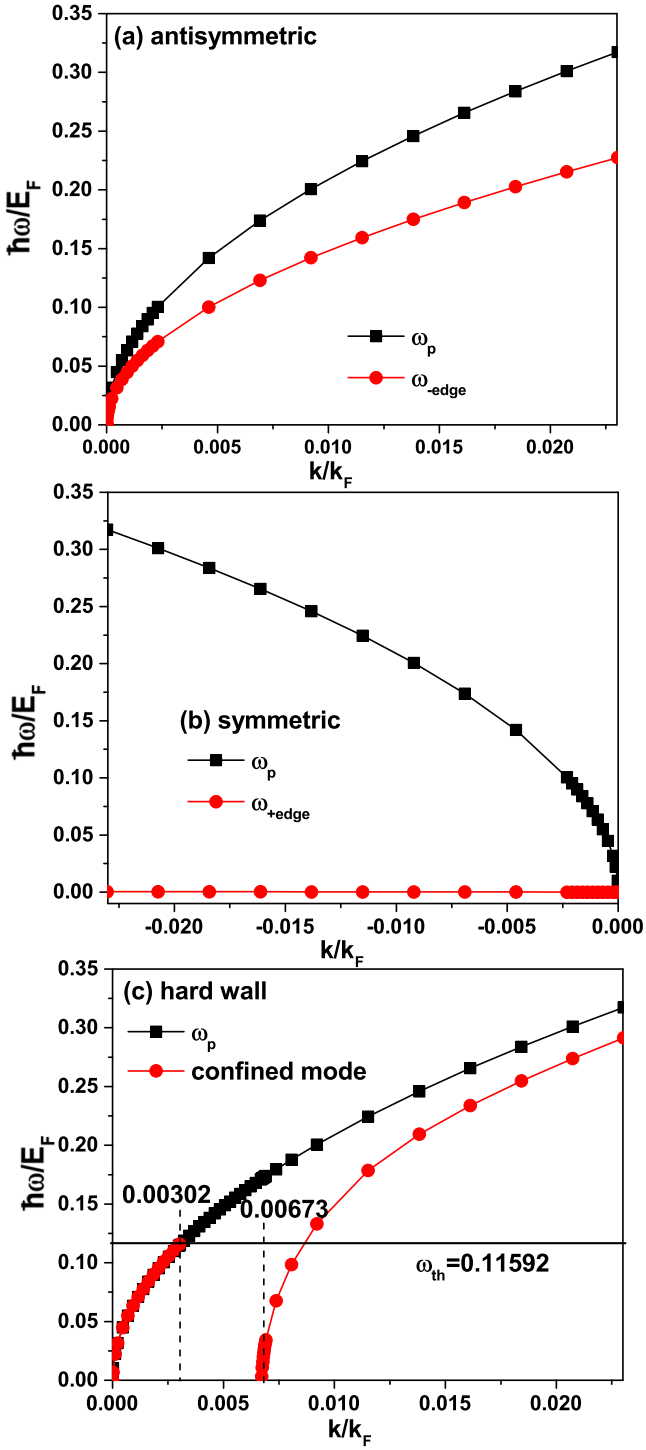

FIG. 2. (a),(b) Dispersion of chiral edge plasmons in an armchair nanoribbon with antisymmetric or symmetric boundary conditions. (c) Dispersion of confined modes in a zigzag nanoribbon under hard-wall boundary conditions. The dispersion of the bulk plasmon ω_{P} (squares) is plotted for comparison. The parameters are $F = 1$ and $L = 1212.5a_0$ ($L = 24a_0$) for the zigzag (armchair) nanoribbon. No confined mode is found in the AC nanoribbon.

the same as the bulk plasmon dispersion under the threshold frequency $\omega_{\mathrm{th}} = 0.115\,92E_F/\hbar$ and it has a frequency gap within $0.003\,02 < |k|/k_F \leqslant 0.006\,73$. The calculation step of the wave number is $0.000\,02k_F$ near the gap, which substitutes the maximum error of 0.3% for determining the lower and upper bound of the gap. There is no real solution in the gap. Here the gap formation is similar to that in the semi-infinite case (see the $\omega_{-\mathrm{edge}}$ branch in Ref. [24]). By comparing the results in [23,24], it can be seen that such a gap is caused by the second term ($\propto \nabla n_{e1}$) on the right side of Eq. (2). Thus the confined mode for ZZ GNR exists only at proper frequencies and wave numbers, which is also predicted theoretically [17]. In a recent experiment [41], confined plasmon modes in ZZ GNRs were revealed from the enhanced near-field optical response near the ZZ edges. Such a signal is not observed near the AC edges.

We now compare the one-way edge modes in AC nanoribbons and one-way confined modes in ZZ nanoribbons with edge plasmons in a semi-infinite geometry calculated in our previous work [24]. The frequencies of edge plasmons in AC nanoribbons ($\omega_{-\mathrm{edge}}$ and $\omega_{+\mathrm{edge}}$) are always lower than the bulk-plasmon frequency ω_{P}. This fact is useful for enhancing the lifetime of the edge mode propagating along the ribbon edge. In contrast, the one-way confined mode in ZZ nanoribbons presents a frequency gap and has frequency $< \omega_{\mathrm{P}}$ at the right side of the gap region, which is very similar to the $\omega_{-\mathrm{edge}}$ mode of the semi-infinite system [24]. Its plasmon frequency almost coincides with ω_{P} at small wave vector k. This nonreciprocal waveguide at the nanoscale could have potential applications for nonreciprocal devices without a magnetic field.

Edge plasmon modes in GNRs have also been proposed theoretically [42] and reported experimentally [6,10]. Kumar *et al.* [42] predicted one-way edge modes with a valley-dependent propagation direction, which shows some characteristics similar to our results. However, in their work, the one-way edge modes have a symmetric dispersion due to spatial symmetry [43]. Fei *et al.* [10] observed peculiar one-dimensional modes propagating along the ribbon edges in infrared nanoimaging experiments, where the plasmon fringe patterns changed upon varying the infrared frequencies. In addition, Nikitin *et al.* [6] imaged a dipole's near-field structure of edge-plasmon modes by using scattering-type scanning near-field optical microscopy with the dipole located at different positions inside and at the boundary of the GNR. In these experiments, the edge modes are strictly confined to the ribbon edges, which is confirmed by our results.

The transverse confinement length of these one-way plasmon modes, defined as the ratio $|k/k_n|$, is plotted in Fig. 3. The parameters of Figs. 2 and 3 are the same. For the edge plasmons in the AC GNR, the electrostatic potential ϕ decays exponentially from the edges to the center, as shown in Fig. 3(a). For the confined mode in the ZZ GNR under condition $\mathbf{V}(y = \pm L/2) \equiv 0$, the potential ϕ varies sinusoidally from one edge to the other [see Fig. 3(b)]. As shown in Figs. 3(c) and 3(d), for the edge-plasmon mode $\omega_{-\mathrm{edge}}$ in AC GNR and the confined mode in ZZ GNR, the transverse confinement length is lower than 0.1 in the considered region of the wave vector. It tends to zero for $|k| \to 0^+$. The transverse confinement length in this case is an order of magnitude smaller than that in a semi-infinite system [24], which is helpful to achieve optical nonreciprocity in GNRs without a magnetic field. For the edge-plasmon mode $\omega_{+\mathrm{edge}}$ in AC GNRs, the transverse confinement length changes slightly around the

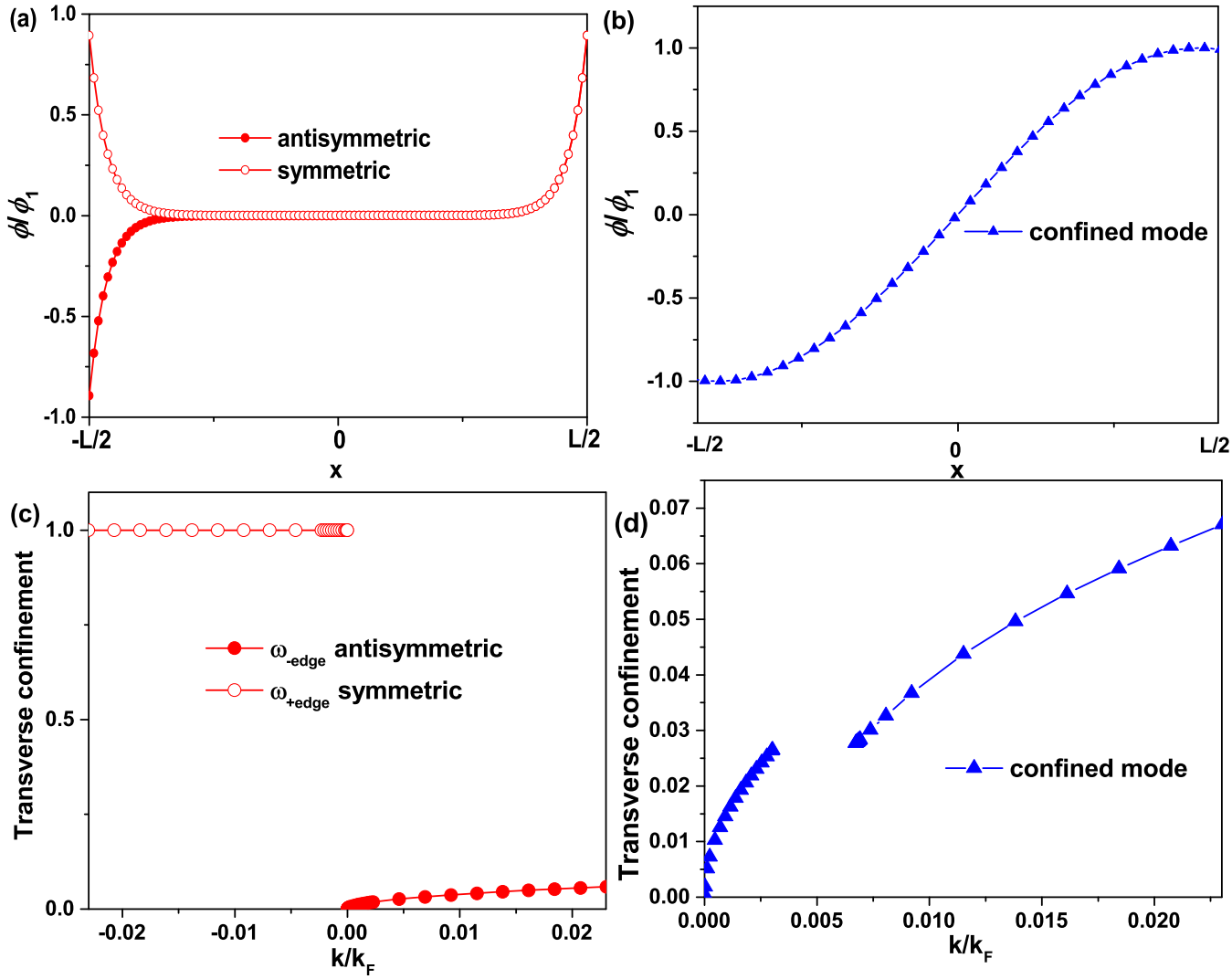

FIG. 3. (a),(b) Normalized electric potential ϕ/ϕ_1 and (c), (d) transverse confinement length $|k/k_n|$ for chiral edge plasmons and confined mode. In panels (a) and (c), the armchair nanoribbons are considered under antisymmetric or symmetric boundary conditions, whereas, in panels (b) and (d), zigzag nanoribbons are considered under hard-wall boundary conditions. The parameters of Figs. 2 and 3 are the same. The electric potential ϕ under edge-plasmon modes $\omega_{\pm\text{edge}}$ decays rapidly from the edges to the center. Under the confined mode, ϕ displays a sinusoidal variation. The transverse confinement length of the $\omega_{-\text{edge}}$ branch (<0.1) is much less than that of the $\omega_{+\text{edge}}$ branch (≈ 1). Similar to the $\omega_{-\text{edge}}$ edge mode in the armchair nanoribbon, the confined mode in the zigzag ribbon is strongly localized near the edge ($|k/k_n|<0.1$).

constant 1. The localization of plasmon-induced potential near the edges requires $|k_n L|>1$. For a given propagating wave vector k, the $\omega_{-\text{edge}}$ mode and the confined mode can appear under $L\approx 0.1/|k|$, while the $\omega_{+\text{edge}}$ mode appears only under $L \gtrsim 1/|k|$.

It has been reported [6,10,22,42] that the ribbon width can influence the properties of edge plasmons. In Figs. 4(a) and 4(b), the dispersion of the edge plasmons in AC ribbons is plotted for different values of ribbon width L. Under antisymmetric boundary conditions [Fig. 4(a)], the edge-plasmon frequency $\omega_{-\text{edge}}$ can exceed the bulk plasmon frequency ω_{P} (at large wave vector) for $L = 720a_0 = 177$ nm. However, the frequency $\omega_{-\text{edge}}$ is always less than ω_{P} for a smaller L. In this case, this type of edge-plasmon mode may be applicable for GNR plasmonics due to its small transverse confinement length (<0.1). Under symmetric boundary conditions [Fig. 4(b)], the edge-plasmon frequency $\omega_{+\text{edge}}$ is less than ω_{P} over the entire wave-vector region considered, even for a large ribbon width $L = 24\,250a_0 = 6$ μm. With increasing the ribbon width, the edge-plasmon frequency approaches the bulk value ω_{P} globally. For the confined mode in ZZ ribbons under hard-wall boundary conditions, the plasmon frequency at a fixed wave vector $k = 0.023$ is plotted as a function of ribbon width. The frequency decreases monotonically with increasing ribbon width, which is similar to the eigenenergy of electron edge states in ZZ GNR [15]. In contrast, in AC ribbons the edge-plasmon frequency $\omega_{\pm\text{edge}}$ increases generally as the ribbon width increases. Such a difference arises from the boundary-condition dependence of one transcendental equation used to determine the dispersion relation.

Due to time-reversal symmetry, the Berry curvature has opposite signs for electrons in the K and K' valley. Electrons in the K (K') valley are subject to the Berry flux $F_K>0$ ($F_{K'} = -F_K<0$). Naively, the two valleys are treated

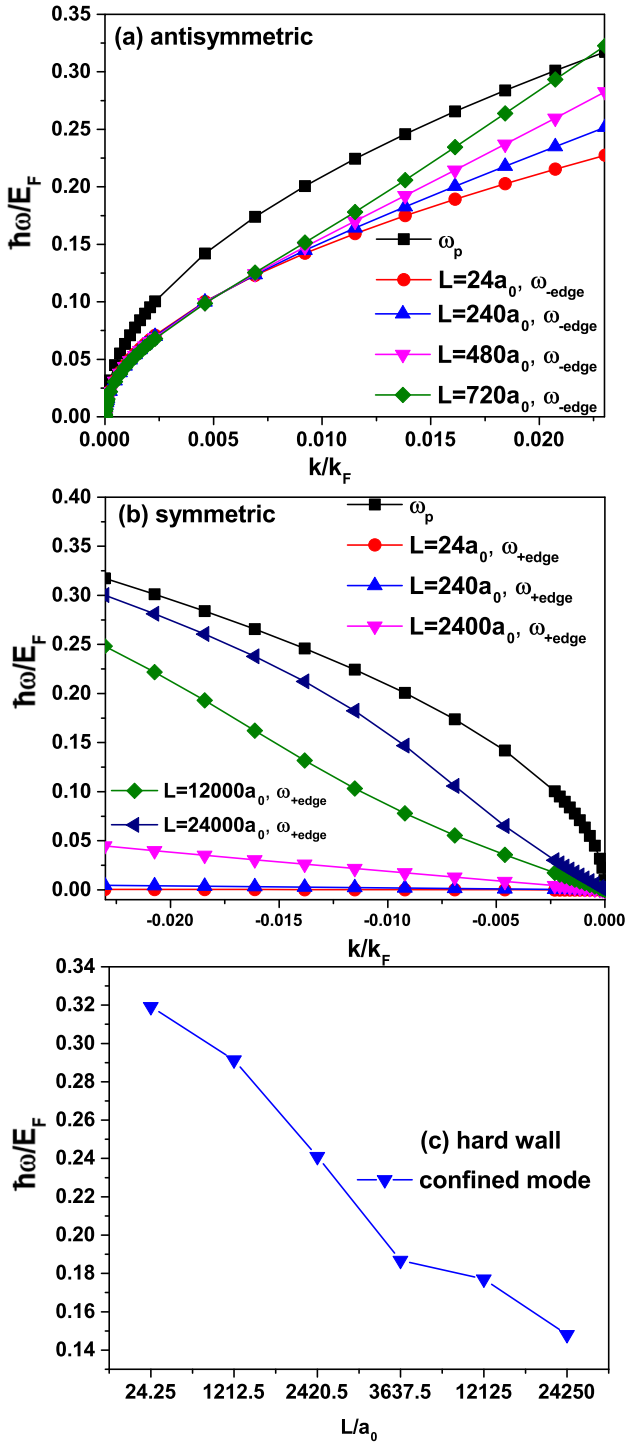

FIG. 4. (a),(b) Dispersion of chiral edge plasmons in armchair nanoribbons under antisymmetric and symmetric boundary conditions for different ribbon widths. The dispersion ω_P of the bulk plasmon is plotted as squares for comparison. (c) Frequency of confined mode in zigzag nanoribbons under hard-wall boundary conditions plotted as a function of ribbon width L. The wave number k is fixed at $|k| = 0.023$. In all panels, the Berry flux is set at $F = 1$.

separately in the present work. Figure 5 demonstrates the effect of Berry flux F on the edge plasmons for both the K and K' subsystem under different boundary conditions. The wave vector is fixed at $|k| = 0.023$ at which $\omega_p \approx 0.32$. The width of

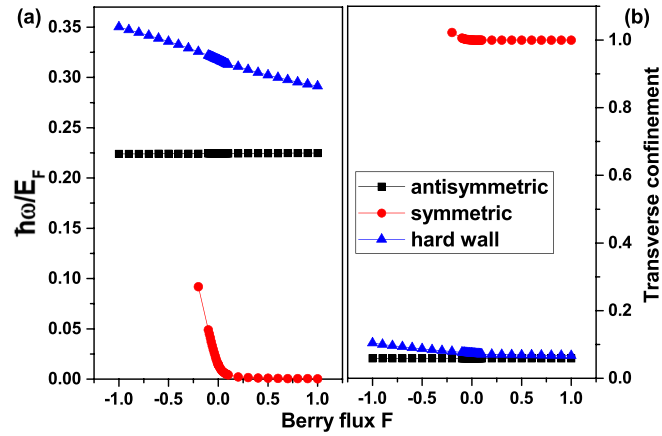

FIG. 5. (a) Frequency ω and (b) transverse confinement length $|k/k_n|$ plotted as functions of the dimensionless Berry flux F. The three curves are for edge plasmons in armchair ribbons under antisymmetric (square) and symmetric (circle) boundary conditions and for confined modes (up-triangle) in zigzag ribbons under hard-wall boundary conditions. The wave number $|k|$ is fixed at 0.023 at which $\omega_p \approx 0.32$. The ribbon width is $L = 24a_0$ ($L = 1212.5a_0$) for the armchair (zigzag) nanoribbon.

the ribbon is set as $L = 24a_0$ ($L = 1212.5a_0$) for the AC (ZZ) ribbon.

It is evident that the Berry flux F has a different influence on the edge plasmons for AC and ZZ GNRs. For the K' subsystem in AC GNR ($F<0$), with increasing $|F|$, both the frequency and the transverse confinement length of the $\omega_{+\text{edge}}$ mode (under symmetric boundary condition) decrease quickly, while those of the $\omega_{-\text{edge}}$ mode (under antisymmetric boundary condition) is almost unchanged. For the K subsystem in AC GNR ($F>0$), both the frequency and the transverse confinement length of edge modes $\omega_{\pm\text{edge}}$ are almost unchanged by the Berry flux. This indicates that the presence of edge plasmons in AC GNRs is almost independent of the strength of Berry flux. For ZZ GNR, with increasing $|F|$, both the frequency and the transverse confinement length of the confined mode (under the hard-wall boundary condition) increase (decrease) for the K' (K) subsystem. This feature agrees with the results in Ref. [23]. It is also seen that the transverse confinement length for the $\omega_{-\text{edge}}$ mode in AC GNR is always smaller than that for the confined mode in ZZ GNR. This feature has been experimentally reported by Duan *et al.* [41], and now our theoretical result confirms it.

IV. CONCLUSION

In this paper, we use a quantum hydrodynamic method to investigate chiral Berry plasmons in graphene nanoribbons with zigzag or armchair edges. A finite Berry flux and Fermi pressure are considered simultaneously. The results indicate that a one-way acoustic edge mode exists in armchair ribbons under antisymmetric or symmetric boundary conditions, whereas a confined mode occurs in zigzag ribbons under hard-wall boundary conditions. The analytical dispersion relations and the transverse confinement length are derived for edge and confined plasmon modes. At a small ribbon width, the

frequencies of edge-plasmon modes and confined modes are always lower than the bulk plasmon frequency. In contrast, the edge-plasmon dispersion in a semi-infinite structure can intersect the bulk plasmon dispersion. For edge-plasmon modes in armchair ribbons under symmetric boundary condition and confined modes in zigzag ribbons, the transverse confinement length is an order of magnitude less than that in a semi-infinite structure. The boundary condition for ribbon edges can greatly alter the dispersion and the transverse confinement of chiral Berry plasmons in graphene nanoribbons. These superconfined one-way edge-plasmon or confined modes are useful for optoelectronic and nanophotonic applications and are relevant for realizing optical nonreciprocity and developing highly sensitive spectroscopy without magnetic fields.

ACKNOWLEDGMENTS

This work was supported by the Natural Science Foundation of China through Grants No. 11775164 and No. 11774314 and the Fundamental Research Funds for the Central Universities through Grants No. 2017IVA79, No. 2018IB011, No. 2018IB009, and No. 2017IB013.

APPENDIX: DETAILS ON EQS. (8)–(12)

In this Appendix, we present a detailed derivation of Eqs. (8)–(12). In the long-wave-length limit [2,23], the nonlocal kernel $W_k(y)$ with Fourier transform $W_k(q)$ can be well approximated by a local kernel $\hat{W}_k(y)$ with Fourier transform $\hat{W}_k(q)$, where

$$\begin{aligned} W_k(y) &= \int \frac{dq}{2\pi} W_k(q)\exp(iqy), \\ W_k(q) &= (-2\pi e/\kappa)|q^2+k^2|^{-1/2}, \\ \hat{W}_k(q) &= (-2\pi e/\kappa)\times 2|k|/(q^2+2k^2). \end{aligned} \tag{A1}$$

In these expressions, k is the wave vector of the edge plasmon and can be negative. As emphasized in Ref. [2], the exact and approximate Fourier transforms of $W_k(y)$ for $k\neq 0$ must have the same first two terms in a power series about $q^2=0$, that is, $|W_k(q)-\hat{W}_k(q)|=O(q^4)$. This requirement explains why it is the factor $|k|$ rather than k that appears in $\hat{W}_k(q)$. The approximate kernel $\hat{W}_k(y)=\int \frac{dq}{2\pi}\hat{W}_k(q)\exp(iqy)$ can be written as $-2(e/\kappa)|k|A$, where

$$A=\int \frac{dq\exp(iqy)}{q^2+2k^2}=\int \frac{dq\cos(qy)}{q^2+2k^2}=\int \frac{dq\exp(iq|y|)}{q^2+2k^2}. \tag{A2}$$

Here we have used the identity $\exp(iqy)=\cos(qy)+i\sin(qy)$ and $\int \frac{dq\sin(qy)}{q^2+2k^2}=0$. The integral A is calculated directly by the residue theorem on the complex-variable function $f(q)=\frac{\exp(iq|y|)}{q^2+2k^2}$. Note that $f(q)$ has only one pole $q_0=\sqrt{2}|k|i$ in the upper half q-plane and satisfies Jordan's Lemma (since $|y|\geqslant 0$). One has $A=2\pi i\,\mathrm{res}\, f(q_0)=2\pi i\frac{\exp(iq|y|)}{2q}|_{q=q_0}=\frac{\pi\exp(-\sqrt{2}|ky|)}{\sqrt{2}|k|}$. This gives $\hat{W}_k(y)=-\frac{4\pi e/\kappa}{2\sqrt{2}}\exp(-\sqrt{2}|ky|)$. This is the second identity of Eq. (8).

From Eqs. (3) and (5) we get

$$\phi_k(y)=\int dy' W_k(y-y')n_{e1k}(y'). \tag{A3}$$

From the convolution theorem, the Fourier transform of $\phi_k(y)$ reads

$$\overline{F}\{\phi_k(y)\}=\overline{F}\{W_k(y)\}\overline{F}\{n_{e1k}(y)\}. \tag{A4}$$

Here $\overline{F}$ is the Fourier transform operator. With the approximated form $\overline{F}\{W_k(y)\}\approx\hat{W}_k(q)$ and Eq. (A1), one has

$$\overline{F}\{\phi_k(y)\}=-(4\pi e|k|/\kappa)/(q^2+2k^2)\overline{F}\{n_{e1k}(y)\}. \tag{A5}$$

Applying the inverse Fourier transform to

$$(-q^2-2k^2)\overline{F}\{\phi_k(y)\}=(4\pi e|k|/\kappa)\overline{F}\{n_{e1k}(y)\}, \tag{A6}$$

we get

$$\left(\partial_y^2-2k^2\right)\phi_k(y)=4\pi(e/\kappa)|k|n_{e1k}(y) \tag{A7}$$

for $|y|\leqslant L/2$. For $|y|>L/2$, where $n_{e1k}(y)=0$, one has $(\partial_y^2-2k^2)\phi_k(y)=0$. In this way, we obtain Eq. (9), which is one prerequisite for Eq. (12). In the region $|y|\leqslant L/2$, the edge plasmon is assumed to satisfy [2,23]

$$\partial_y^2\phi_k(y)=k_n^2\phi_k(y). \tag{A8}$$

This gives

$$\nabla^2\phi=\left(k_n^2-k^2\right)\phi, \tag{A9}$$

which holds for all considered boundary conditions. The value of k_n depends on the type of boundary conditions.

Applying $\partial/\partial t$ to the continuity relation in Eq. (1), we obtain

$$0 = \frac{\partial^2 n_{e1}}{\partial t^2} + n_0 \nabla \cdot \frac{\partial \mathbf{V}}{\partial t}. \tag{A10}$$

From Eqs. (2) and (4), we get

$$\frac{\partial \mathbf{V}}{\partial t} = \frac{\partial \mathbf{u_e}}{\partial t} + \frac{\partial \mathbf{V_a}}{\partial t} = \frac{e}{m^*}\nabla\phi - \frac{v_F^2}{n_0}\nabla n_{e1} + \frac{eF}{n_0\hbar}\frac{\partial}{\partial t}(\nabla\phi \times \mathbf{e}_z). \tag{A11}$$

Note that the last term in Eq. (2) is neglected [see the argument in the paragraph above Sec. II(A)]. The divergence of the vector $\partial\mathbf{V}/\partial t$ appears in Eq. (A10), which is

$$\nabla \cdot \frac{\partial \mathbf{V}}{\partial t} = \frac{e}{m^*}\nabla^2\phi - \frac{v_F^2}{n_0}\nabla^2 n_{e1} + \frac{eF}{n_0\hbar}\frac{\partial}{\partial t}\nabla \cdot (\nabla\phi \times \mathbf{e}_z). \tag{A12}$$

Here we have used the relation $\nabla \cdot \nabla = \nabla^2$ between the nabla operator ∇ and the Laplacian operator ∇^2. This calculation gives

$$0 = \frac{\partial^2 n_{e1}}{\partial t^2} + n_0\frac{e}{m^*}\nabla^2\phi - v_F^2\nabla^2 n_{e1} + \frac{eF}{\hbar}\frac{\partial}{\partial t}\nabla \cdot (\nabla\phi \times \mathbf{e}_z). \tag{A13}$$

Since $\nabla \cdot (\nabla\phi \times \mathbf{e}_z) = \frac{\partial^2\phi}{\partial x\partial y} - \frac{\partial^2\phi}{\partial y\partial x} = 0$ and $v_F^2 = \frac{\hbar^2\pi n_0}{m^{*2}}$, Eq. (A13) yields Eq. (10).

From Eq. (9) we get Eq. (11), which together with Eq. (A8) leads to

$$\nabla^2 n_{e1} = \left(k_n^2 - k^2\right)n_{e1}, \quad \frac{\partial^2 n_{e1}}{\partial t^2} = -\omega^2 n_{e1}, \quad \nabla^2\phi = n_{e1}\left(k_n^2 - k^2\right)\frac{4\pi e|k|/\kappa}{k_n^2 - 2k^2}.$$

Substituting these expressions into Eq. (10), we obtain Eq. (12).

[1] D. B. Mast, A. J. Dahm, and A. L. Fetter, Phys. Rev. Lett. **54**, 1706 (1985).
[2] A. L. Fetter, Phys. Rev. B **32**, 7676 (1985).
[3] A. L. Fetter, Phys. Rev. B **33**, 3717 (1986).
[4] N. Kumada, P. Roulleau, B. Roche, M. Hashisaka, H. Hibino, I. Petković, and D. C. Glattli, Phys. Rev. Lett. **113**, 266601 (2014).
[5] A. Principi, M. I. Katsnelson, and G. Vignale, Phys. Rev. Lett. **117**, 196803 (2016).
[6] A. Nikitin, P. Alonso-González, S. Vélez, S. Mastel, A. Centeno, A. Pesquera, A. Zurutuza, F. Casanova, L. Hueso, F. Koppens *et al.*, Nat. Photon. **10**, 239 (2016).
[7] P. G. Silvestrov and K. B. Efetov, Phys. Rev. B **77**, 155436 (2008).
[8] J. M. Poumirol, W. Yu, X. Chen, C. Berger, W. A. de Heer, M. L. Smith, T. Ohta, W. Pan, M. O. Goerbig, D. Smirnov, and Z. Jiang, Phys. Rev. Lett. **110**, 246803 (2013).
[9] H. Yan, Z. Li, X. Li, W. Zhu, P. Avouris, and F. Xia, Nano Lett. **12**, 3766 (2012).
[10] Z. Fei, M. Goldflam, J.-S. Wu, S. Dai, M. Wagner, A. McLeod, M. Liu, K. Post, S. Zhu, G. Janssen *et al.*, Nano Lett. **15**, 8271 (2015).
[11] E.-J. Kan, Z. Li, J. Yang, and J. Hou, Appl. Phys. Lett. **91**, 243116 (2007).
[12] Y. Lu, R. Wu, L. Shen, M. Yang, Z. Sha, Y. Cai, P. He, and Y. Feng, Appl. Phys. Lett. **94**, 122111 (2009).
[13] K. Nakada, M. Fujita, G. Dresselhaus, and M. S. Dresselhaus, Phys. Rev. B **54**, 17954 (1996).
[14] L. Brey and H. A. Fertig, Phys. Rev. B **73**, 195408 (2006).
[15] L. Brey and H. A. Fertig, Phys. Rev. B **73**, 235411 (2006).
[16] L. Brey and H. A. Fertig, Phys. Rev. B **75**, 125434 (2007).
[17] F. Karimi and I. Knezevic, Phys. Rev. B **96**, 125417 (2017).
[18] K. O. Wedel, N. A. Mortensen, K. S. Thygesen, and M. Wubs, Phys. Rev. B **99**, 045411 (2019).
[19] D. R. Andersen and H. Raza, Phys. Rev. B **85**, 075425 (2012).
[20] A. A. Shylau, S. M. Badalyan, F. M. Peeters, and A. P. Jauho, Phys. Rev. B **91**, 205444 (2015).
[21] F. J. Garcia de Abajo, Acs Photon. **1**, 135 (2014).
[22] A. Yu. Nikitin, F. Guinea, F. J. García-Vidal, and L. Martín-Moreno, Phys. Rev. B **84**, 161407(R) (2011).
[23] J. C. Song and M. S. Rudner, Proc. Natl. Acad. Sci. (USA) **113**, 4658 (2016).
[24] Y. Zhang, F. Zhai, B. Guo, L. Yi, and W. Jiang, Phys. Rev. B **96**, 045104 (2017).
[25] F. Haas, G. Manfredi, and M. Feix, Phys. Rev. E **62**, 2763 (2000).
[26] G. Manfredi and F. Haas, Phys. Rev. B **64**, 075316 (2001).
[27] L. Garcia, F. Haas, L. De Oliveira, and J. Goedert, Phys. Plasmas **12**, 012302 (2005).
[28] M. Marklund and G. Brodin, Phys. Rev. Lett. **98**, 025001 (2007).
[29] P. Shukla, Phys. Lett. A **352**, 242 (2006).
[30] C.-Z. Li, Y.-H. Song, and Y.-N. Wang, Phys. Rev. A **79**, 062903 (2009).
[31] Y. Zhang, W. Jiang, and L. Yi, Nucl. Instrum. Methods Phys. Res., Sect. B **349**, 72 (2015).
[32] Z. Mir, M. Shahid, M. Jamil, A. Rasheed, and A. Shahbaz, Phys. Plasmas **25**, 032120 (2018).
[33] F. Haas, *Quantum Plasmas an Hydrodynamic Approach* (Springer, 2011).

[34] A. H. Castro Neto, F. Guinea, N. M. R. Peres, K. S. Novoselov, and A. K. Geim, Rev. Mod. Phys. **81**, 109 (2009).
[35] D. Xiao, W. Yao, and Q. Niu, Phys. Rev. Lett. **99**, 236809 (2007).
[36] D. Xiao, G.-B. Liu, W. Feng, X. Xu, and W. Yao, Phys. Rev. Lett. **108**, 196802 (2012).
[37] N. Ashcroft and N. Mermin (unpublished).
[38] G. Tkachov, Phys. Rev. B **79**, 045429 (2009).
[39] K.-i. Sasaki, K. Wakabayashi, and T. Enoki, J. Phys. Soc. Jpn. **80**, 044710 (2011).
[40] M. Moradinasab, H. Nematian, M. Pourfath, M. Fathipour, and H. Kosina, J. Appl. Phys. **111**, 074318 (2012).
[41] J. Duan, R. Chen, Y. Cheng, T. Yang, F. Zhai, Q. Dai, and J. Chen, Adv. Mater. **30**, 1800367 (2018).
[42] A. Kumar, A. Nemilentsau, K. H. Fung, G. Hanson, N. X. Fang, and T. Low, Phys. Rev. B **93**, 041413(R) (2016).
[43] R. Camley, Sur. Sci. Rep. **7**, 103 (1987).